Directed Energy Beam Improvement Using Binary Control for the Advanced Tactical Laser (DEBI-BATL)

William W. Bower, Valdis Kibens,
The Boeing Company, MC S306-430,
P.O. Box 516, Saint Louis, MO 63166

David A. Nahrstedt,
The Boeing Company, MC S306-430,
8531 Fallbrook Ave., West Hills, CA 91304

Bojan Vukasinovic, Ari Glezer,
Woodruff School of Mechanical Engineering,
Georgia Institute of Technology, Atlanta, GA 30332-0405

Stanislav Gordeyev, Eric Jumper,
Department of Aerospace and Mechanical Engineering,
University of Notre Dame, Notre Dame, IN 46556

Donnie Saunders
Air Force Research Laboratory/RBAI,
Wright-Patterson AFB, OH 45433-7542

The effects of direct small-scale actuation on the aerodynamic and aero-optical characteristics of the flow over a hemisphere-on-cylinder turret model (D = 0.61 m) with a round 0.254 m diameter conformal optical window are investigated at M = 0.3 and $Re_D = 4.46 \cdot 10^6$ (with additional measurements at M = 0.4 and 0.5). Flow control is effected by arrays of piezoelectrically-driven synthetic jet modules. The cumulative effect of the actuation is manifested by concomitant delay of flow separation and active, dissipative suppression of turbulent motions downstream of separation. The effects of actuation on aero-optical distortions are assessed from the flow dynamics using surface oil visualization, static pressure distributions and hot-film measurements within the separated flow domain. In addition, the suppression of optical distortions across the separated flow is measured directly using a Malley probe over a range of elevation angles. These measurements show that for a fixed actuation level, the active suppression of spectral components of the optical distortion is about 30% within a resolved frequency band 0.5 < f < 25 kHz at M = 0.3.

Keywords: turret, flow control, aberrations, optical mitigation

Nomenclature

A_j = exit area of the actuator orifice
A_o = frontal turret area
Ap = aperture size
Cp = pressure coefficient

C_μ = jet momentum coefficient
D = turret diameter
f_d = actuation frequency
I = far-field intensity
I_0 = diffraction-limited intensity
k = turbulent kinetic energy
M = Mach number
OPD = optical path difference
OPD_{rms} = root-mean-square of OPD
R = turret radius
Re_D = Reynolds number
St_D = Strouhal number
U_0 = free stream velocity
U_j = average jet velocity
W_{rms} = wavefront mean-removed spatial root-mean-square
H = height of turret base
β = azimuthal angle of pressure ports
γ = elevation angle of optical window
γ_s = flow separation angle
λ = wavelength
ρ = air density

I. Background

Turrets provide convenient housing for pointing and tracking laser beams from airborne platforms. However, a turret creates a separated turbulent region of the flow, which, even at relatively-low subsonic speeds, starts to distort an otherwise planar emerging laser beam (e.g., Sutton 1985, Gordeyev *et al.* 2007). This, in turn, leads to the laser beam's unsteady defocus and jitter at the target (Gilbert and Otten 1982). Control of the flow over a bluff-body turret that houses a laser-based optical system must satisfy more demanding requirements in comparison to separation control over external aerodynamic surfaces. Whereas the effectiveness of the flow control method on aerodynamic surfaces can be evaluated in terms of its effect on the time-averaged aerodynamic forces and moments, the metric becomes much more stringent when the intent of flow control is to enhance transmission of optical wavefronts through regions of separated turbulent flow. When an optical wavefront passes through a variable index-of-refraction turbulent flow near an aerodynamic surface (boundary layers, separated shear layers and wakes), its wavefront becomes distorted or aberrated and these distortions are referred as an *aero-optical problem* (Gilbert and Otten 1982). These wavefront distortions combined with optical aberrations caused by the wavefront propagation through the atmosphere, known as an *atmospheric propagation problem* (Tatarskii and Zavorotnyi 1985), ultimately degrade the light intensity from the otherwise diffraction-limited intensity at the destination. These aberrations have high spatial and temporal bandwidths which are well outside the current capabilities of traditional adaptive-optic methods (Jumper and Fitzgerald 2001). Separated shear layers are particularly destructive because of the presence of coherent vortical structures that induce strong pressure and density gradients (Fitzgerald and Jumper 2004). Left untreated, these shear-layer-related optical aberrations can limit an airborne transmitting system to a forward-looking quadrant only. In order to extend viewing angles to at least a portion of an aft-looking quadrant,

one can extend the region of the attached flow by delaying the separation of the shear layer and/or disrupting formation of the large-scale shear layer vortices. The intent of the work presented in this paper is to evaluate the effectiveness of a strategy for achieving significant improvement in light transmission efficiency by minimizing laser wavefront degradation through active flow control suppression of the unsteady aerodynamic environment, which left untreated leads to serious degradation of the optical environment in uncontrolled flow.

Traditional active method for controlling separation over lifting surfaces and bluff bodies makes use of the strong entrainment properties of the separated shear layer when it is excited at its unstable frequency. Introducing perturbation signals at the nominal (dimensionless) frequency St = O[1] upstream of the region of separation results in enhanced entrainment and a Coanda-like deflection of the flow towards the adjacent aerodynamic surface. However, the deflected flow can separate again depending on the modified streamwise pressure gradients along the surface. While resulting in considerable changes in global aerodynamic forces, this method can degrade an optical signal that is transmitted through the affected region perhaps even beyond the levels observed in the absence of control. A body of work studying the control of separation by the application of actuation at frequencies that are at least an order of magnitude higher than the unstable frequency of the shear layer suggests that high-frequency actuation makes it possible to achieve attached flows in which large coherent vertical motions that are associated with low-frequency actuation are largely suppressed (e.g., Smith *et al.* 1998 and Amitay and Glezer 2002).

Some previous work on separated flows over a three-dimensional bluff-body configuration has been directly motivated by the aero-optical problems involving an aircraft turret. Such a configuration typically consisted of a cylindrical base having a hemispherical cap with a flat or a conformal aperture. The resulting flow field is fairly complex as shown by de Jonckheere et al. (1982). It has been shown (Gordeyev *et al.* 2007 and Cress *et al.* 2007) that the main cause of aero-optical distortions for moderate back-looking angles is the shear-layer structures that form shortly after the flow separates from the hemispherical portion of the turret. Investigations of flow control on these configurations included the effect of suction on the wake structure (Purhoit *et al.* 1983) and the addition of aft-mounted fairings and splitter plates (Snyder *et al.* 2000). The former showed significant alteration of the wake structure even at low levels of suction, while the latter presented reduction of the baseline drag up to 55% by using a large fairing. The separated flow behind the turret with a flat aperture and the effects of passive control on the optical aberrations were characterized by Gordeyev et al. (2005), while the aerodynamical and aero-optical characterization of the baseline flow field over a conformal-window turret configuration was investigated by Gordeyev *et al.* (2007). There have been few investigations of generic surface-mounted hemispheres at high Reynolds numbers. In a numerical investigation of winds over hemispherical domes, Manhart (1998) found that Karman-like vortex train is shed from the hemisphere. In these flows however, the thickness of the upstream boundary layer is comparable to the hemisphere radius, unlike the flow over an aircraft turret for which the oncoming boundary layer thickness is much smaller than the turret radius. Another limiting case, when the cylindrical base is much higher than the hemisphere radius was investigated by Leder *et al.* (2003, $H = 3R$). They characterized the wake behind such a high aspect ratio turret and showed that it is dominated by vortices shed off the cylindrical support. The effectiveness of direct, high-frequency control ($St_D > 10$) of the separated flow over a hemispherical turret on a flat plate with a thin upstream boundary layer was demonstrated by Vukasinovic *et al.* (2005) at $Re_D = 4 - 7 \cdot 10^5$. These authors showed that the presence of flow control can substantially reduce the extent of the recirculating domain downstream of the hemisphere with significant reduction

in turbulent kinetic energy. Vukasinovic et al. (2008) simultaneously measured the aerodynamic and aero-optical environment within the separated flow off a hemispherical turret at free stream Mach-number speeds up to $M = 0.64$. They reported significant suppression of turbulent fluctuations and reduction in optical distortions up to $M = 0.45$ by the active flow control, where reduction in optical distortions at $M = 0.4$ was reported up to 45%. Recently, Woszidlo, Taubert, and Wygnanski (2009) reported separation delay and turbulence intensity reduction within the wake of a hemispherical shell by means of the base suction and upstream passive vortex generators at $Re_D \leq 3 \cdot 10^5$. Vukasinovic and Glezer (2007) demonstrated the effectiveness of fluidic, direct high-frequency control in turbulence suppression behind a bluff-body turret at $Re_D = 8 \cdot 10^5$. Morgan and Visbal (2009) presented numerical simulation of the separation delay over a turret at $M = 0.4$ and $Re_D = 2.4 \cdot 10^6$, and concluded that either localized or distributed suction resulted in significant separation delay and suppression of large-scale structures in the wake.

The present paper reports the effects of direct small-scale excitation on the aerodynamic and aero-optical characteristics within the near wake of a hemisphere-on-cylinder turret model. The actuation using arrays of synthetic jet actuators placed upstream of the turret aperture results in concomitant delay of flow separation and active, dissipative suppression of turbulent motions within the separated shear layer. The effects of the actuations are investigated over a range of optical window elevation angles and are characterized using surface pressure measurements and hot-film anemometry within the separated flow. In addition, direct measurements of aero-optical distortions are assessed using Malley probe measurements. While the primary objective of the current work is to estimate the effectiveness of active flow control for suppression of optical aberrations at $M = 0.3$, the control effectiveness was also assessed at $M = 0.4$ and 0.5. The experimental setup and procedures are described in Section II. The characterization of the base flow is described in Section III, while Section IV presents the results of controlled flow, and finally, the conclusions are presented in Section V.

II. Experimental Setup and Diagnostics Procedures

The present turret model is shown in Figure 1. It measures 0.61 m in diameter, and is equipped with a 0.254 m diameter spherical window insert that models a conformal optical window and therefore this area is unavailable for the flow control hardware. The tunnel blockage imposed by the turret was 4.2%. While the cylindrical turret base ($H/R = 0.625$) remains stationary, the spherical portion of the turret can be rotated about the z-axis for about 53°, thus allowing variation in the window's elevation angle γ (defined as the angular position of the window's

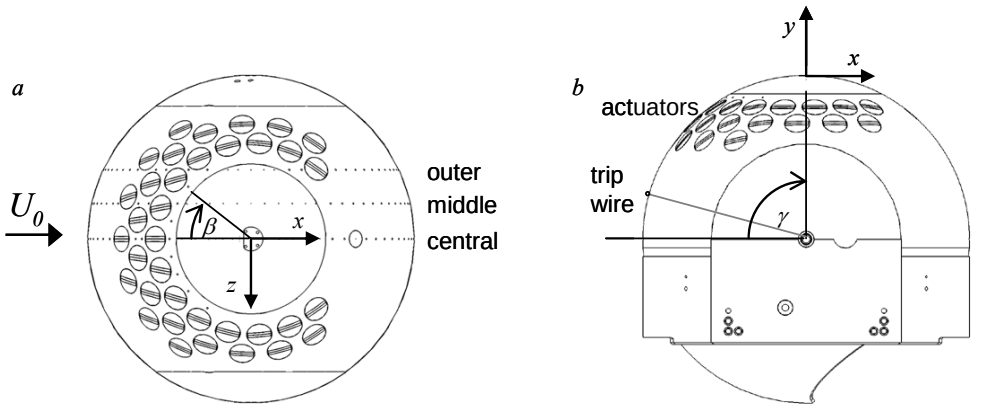

Figure 1. *Top (a) and side (b) views of the 0.61 m dia. turret model having a 0.254 m instrumented spherical cap in place of an optical window.*

centerline, relative to the free stream). The spherical portion of the turret is instrumented with static pressure ports that are distributed along central, middle (20° off centerline), and the outer (40° off centerline) planes (Figure 1), which include 39, 44, and 39 ports, respectively. In addition to these main pressure ports, nine static pressure ports also are distributed just upstream from the optical window, such that the middle port is in the central plane, and four pressure ports are distributed over each half of the window, having azimuthal angles β = 12.5°, 25.6°, 39.7°, and 57.7°. These additional nine ports are used to assess the flow symmetry and spanwise (z-direction) effects of the actuation.

A total of 36 individually-addressable actuators are distributed in three rows around the window circumference, such that the first row (closest to the window) consists of 15, the second of 14, and the third of 7 actuators (Figure 1). Each actuator module has a high aspect ratio rectangular jet orifice (measuring 38.1 × 0.5 mm) that can be rotated about its own axis to allow different orientations of the jet orifice relative to the free stream, thus enabling predominantly streamwise or spanwise vorticity generation upon jet activation. Previous studies suggested possible advantages of the manipulation of spanwise vorticity concentrations in incompressible flows (Vukasinovic and Glezer 2007), and of streamwise vorticity in compressible flows (Vukasinovic *et al.* 2008). In the preliminary stages of the present investigation several combinations of orifice orientations were tested (i.e., aligned with the free stream, approximately with the local flow, and normal to the free stream), and based on these tests it was decided to arrange orifices approximately aligned with the free stream. Since the actuators move with the spherical part of the turret and the optical window, their position relative to the point of separation changes and therefore different actuator arrays can be activated depending on the windows position. In the present experiments, the actuation frequency was kept at f_d = 1,600 Hz, while the actuation strength was varied over $3\cdot10^{-6} < C_\mu < 1.5\cdot10^{-5}$ per single active actuator, as the jet momentum coefficient is defined as $C_\mu = \rho U_j^2 A_j/(\rho U_0^2 A_o)$, where A_j is the total jet orifice area, A_o is frontal projection of the turret, and U_j is the average jet velocity during the expulsion part of the cycle. Three nominal orientations of jet orifices relative to the free stream flow were tested: aligned with the free stream, normal to the free stream, and normal to the optical window center. Control effectiveness was assessed using both the full 36 actuator configuration (maximum $C_\mu = 5.6\cdot10^{-4}$) and the center 24 actuators (maximum $C_\mu = 3.7\cdot10^{-4}$). The former is labeled as *case 1* and latter as *case 2* in the reminder of the paper.

Spectral characterization of the baseline (non-actuated) and actuated flows were accomplished using single-sensor hot wire anemometry. For that purpose, four hot-wire probes were mounted on retractable holders and stowed in a tunnel surface wall depressions when not in use. During the measurements, only one probe at a time was elevated from the surface and positioned at the measurement location, where the cross-stream measurement locations were selected so that the local shear layer thickness was traversed. The sensor streamwise positions are x/R = 0.5 (HW1), 1 (HW2) 1.5 (HW3), and 2 (HW4), where the streamwise distance x is measured from the hemisphere center (Figure 1).

To minimize tunnel-induced mechanical vibrations and relative motion between the turret and the optical bench, inner-tube isolators were placed between the optical table and trusses holding the optical bench, as shown in Figure 2*a*, and they were shown to be effective in reducing the bench's vibrational motion. Optical measurements were performed at the turret center plane (i.e., zenith plane) at four window elevation angles γ = 129°, 137°, 143°, and 148° using the Malley probe. The Malley probe is described in detail by Gordeyev, Hayden, and Jumper (2007); it uses

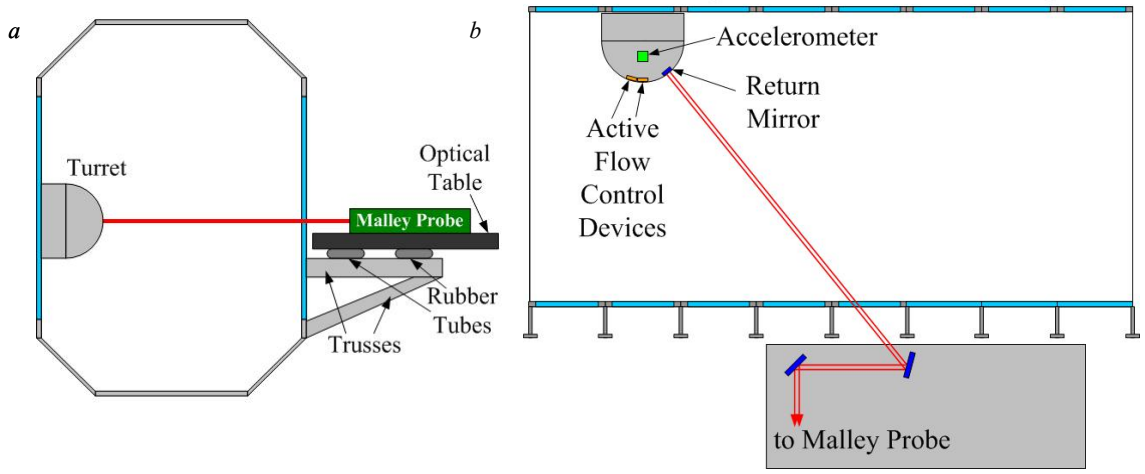

Figure 2. *Optical table arrangement, side (a) and top (b) views.*

two parallel, small-aperture laser beams to measure one-dimensional slices of optical wavefronts in the streamwise direction. Regular Plexiglas windows in the tunnel walls ordinarily would be unacceptable for making optical measurements; however, the Malley probe was able to make optical measurements through these windows because they did not impose significant optical distortions on the small, 1 mm diameter, Malley-probe beams. A round 25.4 mm diameter return mirror was mounted flush on the cap center and two Malley probe He-Ne laser beams were transmitted into the test section using a series of steering mirrors. After reflecting off the surface-embedded return mirror, the beams were reflected back to the optical bench along the same optical path, as shown schematically in Figure 2*b*. This approach in conducting the Malley probe measurements allows the laser beams to go along the same flow twice, doubling the signal-to-noise ratio and significantly simplifying the optical set-up. The Malley-probe laser beams were separated by approximately 7 mm in the streamwise direction. Optical aberrations at selected elevation angles were measured by recording high-bandwidth, time-resolved deflection angles (jitter) of the laser beams using position sensing devices. The sampling frequency used was 50 kHz, and sampling times of 20 seconds were made for each measurement case.

The Malley probe data were processed as follows:

1. Measure streamwise deflection jitter angles $\theta_1(t)$ and $\theta_2(t)$.
2. Compute a cross-correlation function $S(f)$, $S(f) = \left\langle \hat{\theta}_1^*(f)\hat{\theta}_2(f) \right\rangle$, where square brackets denote ensemble averaging and asterisk denotes complex conjugate.
3. Calculate convective speed, U_c, by calculating the time delay between the two jitter signals using the spectral method described by Gordeyev, Hayden, and Jumper (2007).
4. Compute jitter power spectra $P_\theta(f) = \left\langle \left|\hat{\theta}(f)\right|^2 \right\rangle$ for each jitter signal.
5. Remove vibration contamination by analyzing the jitter-angle spectra $P_\theta(f)$ and applying a high-pass filter $F(f)$, as described in the Appendix.
6. Calculate a time varying 1-D wavefront slice, OPD(t), assuming the frozen-flow hypothesis,

$$OPD(t) = -U_c \int \theta_1(t)dt$$

7. Apply an aperture, Ap, to $OPD(t)$ results, remove instantaneous tilt components from each apertured slice and calculate the residual OPD_{rms} average over all ensembles for a given aperture. *Ap*, which was chosen to be 1/3 of the hemisphere diameter, $Ap = 0.2$ m.

III. The Baseline Flow

Earlier investigations (e.g., de Jonckheere 1982, Gordeyev *et al.* 2007, and Vukasinovic *et al.* 2008) have demonstrated that the topology of the baseline turret flow is rather complex, and Mach and Reynolds number-dependent. In order to avoid changes in separation location and dynamics that are associated with the flow transition, the hemisphere's boundary layer in the present experiments was tripped using a 0.2 mm dia. wire which was attached to the surface with a 0.1 mm tape along meridional plane at a 15° elevation relative to the center (symmetry) plane of the hemisphere (Figure 1).

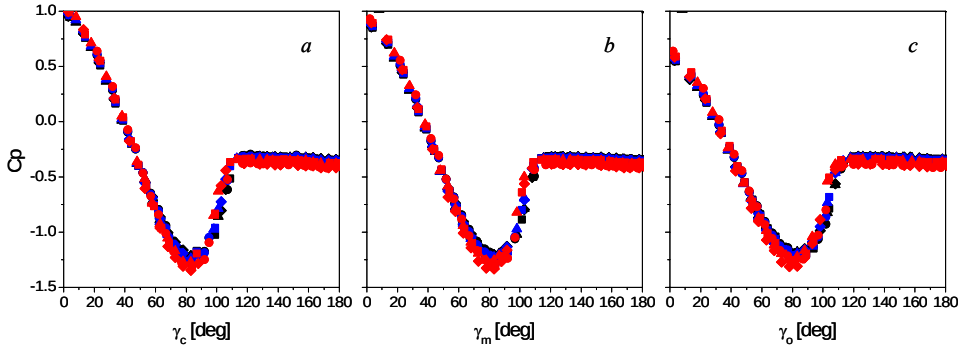

Figure 3. *Overlapped static pressure measurements at window elevation angles γ = 129°, 137°, 143°, and 148°, and baseline flows at M = 0.3 (—), 0.4 (—), and 0.5 (—). in the central (a), middle (b), and the outer (c) planes.*

The tripped baseline flows are first characterized using measurements of static pressure distributions in the central, middle and outer planes shown in Figure 1. The pressure profiles in these three planes are shown in Figure 3 for window elevation angles γ = 129°, 137°, 143°, and 148°, and M = 0.3, 0.4, and 0.5. These pressure profiles suggest that, for a given Mach number, the separation points in each of the three measurement planes nearly coincide at the planes' own reference angles, indicating that the flow separates first over the outer edges of the optical window and remains attached farthest in the central plane. This observation is in accord with previous data reported for the flow over a hemispherical turret (Vukasinovic *et al.* 2008). The present measurements also suggest that the separation angle in all planes shifts slightly upstream with increasing M, such that the flow separates just upstream from 120° in the central plane at M = 0.3, while at M = 0.5, the separation point is at about γ_s = 115°. Perhaps the most interesting view of the baseline flow over the optical window is shown in Figure 4 which includes pressure distributions along the upstream edge

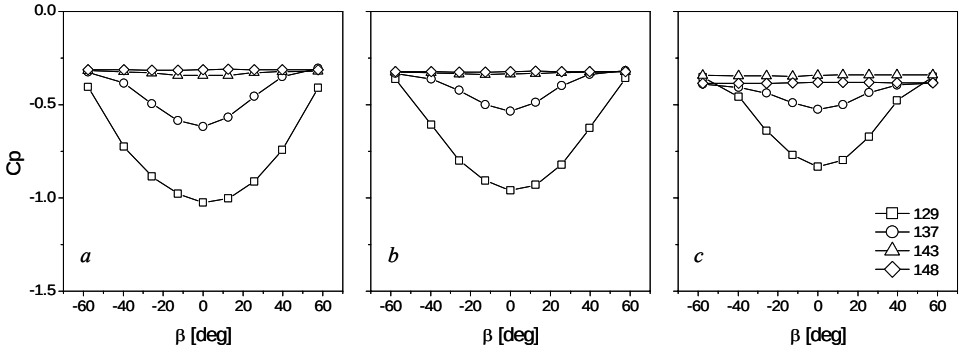

Figure 4. *Pressure distributions about the optical window center (β = 0) at window elevation angle γ = 129° (□), 137° (○), 143° (Δ), and 148° (◊), and for the baseline flows at M = 0.3 (a), 0.4 (b), and 0.5 (c).*

of the window (cf., Figure 1) for $\gamma = 129°$, 137°, 143°, and 148°, and $M = 0.3$, 0.4, and 0.5. These data show that in all of the cases the flow remains remarkably symmetric about the streamwise centerline of the window ($\beta = 0°$). When the flow is not separated at the upstream edge of the window ($\gamma = 129°$ and 137°), the pressure has a minimum at the window center, and increases towards the spanwise edges of the turret. The pressure profiles at $\gamma = 137°$ indicate a presence of a separated flow at the outer upstream edges of the optical window, and at $\gamma = 143°$ and 148°, regardless of M, the flow approaching the optical window is already separated over the measurement domain. The upstream shift in the separation line with increasing M is also apparent in the pressure distributions at the lowest elevation angle, where the approaching flow is attached at $M = 0.3$ and separated at $M = 0.5$.

A global topology of the baseline flow at $M = 0.3$ was investigated using surface oil-flow visualization. The main footprint of the flow was visualized over the flat surface of the supporting turret wall, and additional visualization was performed along the cylindrical turret base. The recorded images of the surface oil visualization showed that the baseline flow over the turret is quite symmetric. Some features of the flow that were educed from these images are shown in schematically in Figures 5*a* (the turret support plane) and 5*b* (the cylinder surface). As the oncoming boundary layer approaches the adverse pressure gradient induced by the presence of the cylinder base, a spanwise (necklace) vortex is formed which becomes strained and deformed under the modified pressure field, giving a rise to the streamwise vortex branches along each spanwise edge of the cylinder. A stagnation point is formed at 0.5R upstream from the turret, the outer flow is displaced by the bluff-body, accelerates over the hemisphere surface and around the cylindrical surface until the adverse pressure gradients on the aft sides induce separation. The flow footprints shown schematically in Figure 5*a* indicate that the flow separates off the cylinder base near its apex, and spreads azimuthally by approximately 120°. The visualization on the surface of the cylinder in Figure 5*b* indicates the 3D nature of the separating flow near the cylinder's base, as well as its localized, near-wall effect. Further away from the support wall, the flow trajectories over the cylinder become displaced towards the hemispherical part of the turret, and merge into a separation line. This visualization supports the assessment, based on the static pressure measurements (Figures 3 and 4), that the flow separates first at the spanwise edges of the turret and remains attached farthest in the (center) plane of symmetry. The ensuing separated flow off the turret surface has a main central wake that reattaches to the support wall at approximately 1.3R downstream from the turret back edge, and two additional near-wall wake segments that appear to be associated with the vortices that are shed off each side of the cylindrical support. After initial narrowing, the main wake begins to spread as shown in Figure 5*a*. It appears that the overall wake dynamics is dominated by the flow separation off the hemispherical

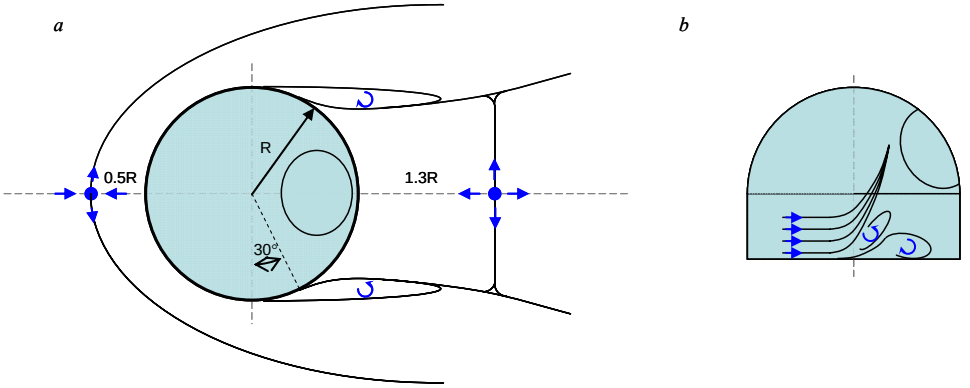

Figure 5. *Schematics of the surface oil-flow visualization of the baseline flow at M = 0.3 at the support wall (a) and cylindrical surface of the turret (b).*

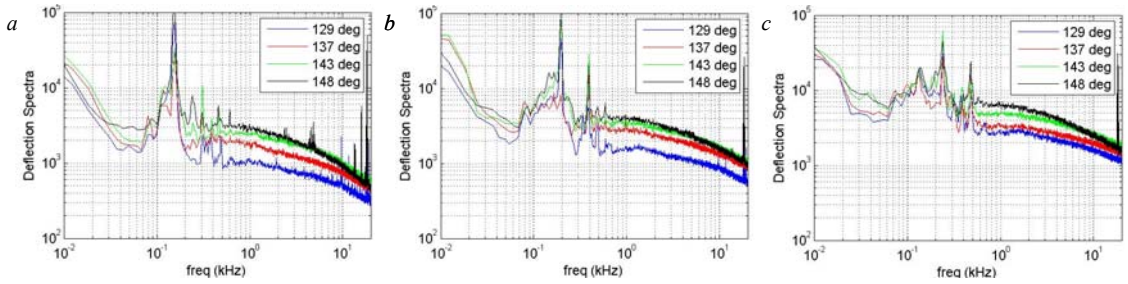

Figure 6. *Optical deflection/jitter-angle spectra as a function of the elevation angle for M = 0.3 (a), 0.4 (b), and 0.5 (c).*

part of the turret, while the separation off the relatively short cylinder base has a limited effect on the wake. In contrast to this observation, measurements in a high aspect ratio turret (Leder *et al.* 2003) where cylindrical base is much taller than its radius, the near wake is dominated by the dynamics of the vortices shed off the cylinder.

Baseline (i.e., turret with no active flow control) Malley probe jitter/beam-deflection-angle spectra for different elevation angles as a function of the incoming Mach number are presented in Figure 6. The series of peaks at low frequencies, below 500 Hz, is the result of mechanical vibrations of the tunnel, the turret, and to a lesser degree the optical bench. For a fixed Mach number, spectra are approximately the same at a range of low frequencies between 80 and 300 Hz, indicating strong tunnel-related mechanical vibrations, which should be independent of the elevation angle. The main vibrational peak is related to the tunnel blade passage speed which was approximately 155 Hz for M = 0.3, 200 Hz for M = 0.4 and 250 Hz for M = 0.5. These vibrations completely overwhelm the optical signal at these frequencies and make the data unusable over that range. Above 500 Hz the optical signal shows a broad hump which indicates the presence of the shear layer behind the turret. For the elevation angle of γ = 129°, the frequency location of this hump increases from approximately 1 kHz to 2 kHz, increasing with Mach number. This characteristic is expected for the shear layer, confirming the fluid-mechanic conclusion that, in the absence of flow control, the Malley-probe beams encounter separated flow at the smallest of the four elevation angles. The corresponding Strouhal number was found to be approximately $St = f_{peak}\, D/U_0$ = 4.5. The location of the shear-layer-related peak moves toward lower frequencies with increasing the elevation angle, indicating that the shear layer grows downstream from the separation location. Intensities of the spectra also increase with the Mach number. The jitter/deflection-angle spectra for a shear layer have been previously shown to follow a "ρM^2"-law (Gordeyev, Hayden, and Jumper 2007, Gordeyev *et al.* 2007). The present spectra further validate this scaling law.

Spectra monotonically increase with increasing the elevation angle, indicating that the optical aberrations caused by the shear layer become stronger with increasing looking-back angle, consistent with the expected optical character of the shear layer. The location of the shear layer peak moves toward lower frequencies with increasing the elevation angle, from 1 kHz to 0.5 kHz for M = 0.3, from 1.3 to 0.8 for M=0.4 and 0.4 and from 1.8 kHz to 0.9 kHz for M = 0.5. Again, this is consistent with the shear layer structures growing in size as they convect downstream. All trends are quite similar to results for optical jitter/deflection-angle spectra around hemispheres (Vukasinovic *et al.* 2008). The increasing optical signal with the elevation angle going up is not only due to the shear layer structures growing downstream (i.e., for a greater look-back angle) but also because of the fact that the laser beam is traversing the shear layer at ever-higher oblique angles, increasing its optical propagation path length due to oblique propagation.

The OPD_{rms} results for the baseline flows are plotted in Figure 7*a* versus $\rho/\rho_{SL}\,M^2$ (ρ_{SL} – sea-level density) for different elevation angles. As can be seen in Figure 7*a* for all elevation angles OPD_{rms} approximately follows the "ρM^2"-dependence. For similar subsonic flows, levels of optical aberrations are proportional to the freestream density, the square of the incoming Mach number and the turret size, D, $OPD_{rms} \sim \rho M^2 D$. To check this self-similarity, the optical results are re-plotted in Figure 7*b* in a self-similar form, $OPD_{rms}\,/((\rho/\rho_{SL})M^2 D)$, versus the elevation angle, γ, for all Mach numbers. Also, the "oblique angle" effect, $OPD_{rms} \sim 1/\sin(\gamma)$ is shown in Figure 7*b* as a dashed line. For all Mach numbers and elevation angles the data approximately collapse about "$1/\sin(\gamma)$"-curve, giving additional validity to the comment made earlier that part of the increase is due to a longer optical path through the shear layer for oblique propagation.

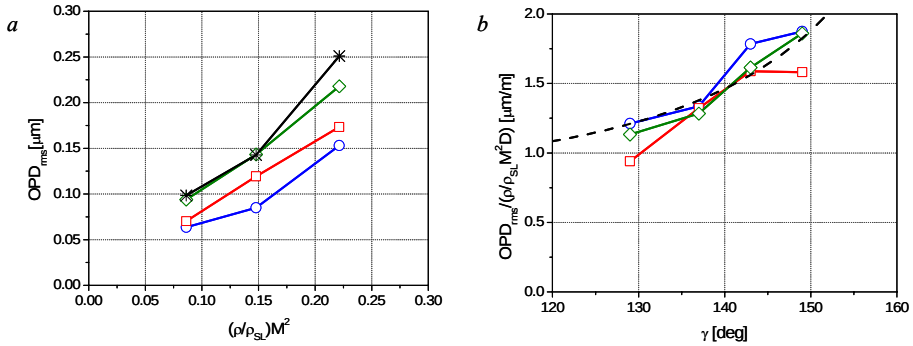

Figure 7. *a) Baseline OPDrms as a function of $\rho/\rho_{SL}M^2$ for different elevation angles γ = 129° (○), 137° (□), 143° (◊), and 149° (∗), and b) Baseline optical data re-plotted in a self-similar form, OPDrms /($\rho M^2 D$) as a function of elevation angles for all Mach numbers M = 0.3 (○), 0.4 (□), and 0.5 (◊). 1/sin(γ) is plotted as a reference (---).*

IV. The Controlled Flow

The effects of the actuation strength in terms of the synthetic jet momentum coefficient on the suppression of turbulent energy within the separated flow domain was assessed by varying the jet exit velocity ($C_\mu < 5.6\cdot10^{-4}$) and measuring the corresponding distributions of static pressure. An example of the measured pressure distributions in three planes is shown in Figure 8 for $\gamma = 139°$ and $M = 0.3$. These data show a clear dependence of streamwise separation delay on the jet momentum coefficient in all three measurement planes and suggests that stronger actuation could lead to additional changes in C_p. The effect of varying the jet momentum coefficient on the spectral properties of the separated flow is demonstrated in Figure 9 at a fixed elevation within the shear layer at all four hot-film measurement stations [x/R = 0.5 (HW1), 1 (HW2) 1.5 (HW3), and 2]. As discussed above, direct actuation of small-scale dissipative motions leads to a significant broad band reduction in turbulent kinetic

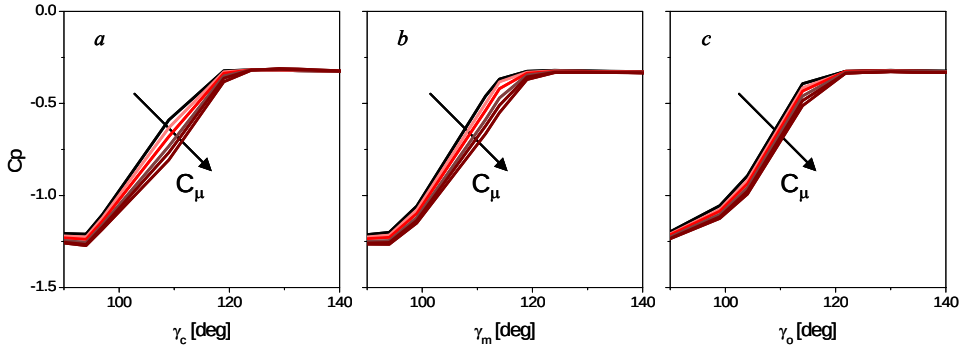

Figure 8. *Static pressure profiles for the baseline flow (—) at M = 0.3 and γ = 139°, and controlled flows in the central (a), middle (b), and the outer (c) planes. Controlled pressure profile is increasingly darker red in color with an increase in the jet momentum coefficient.*

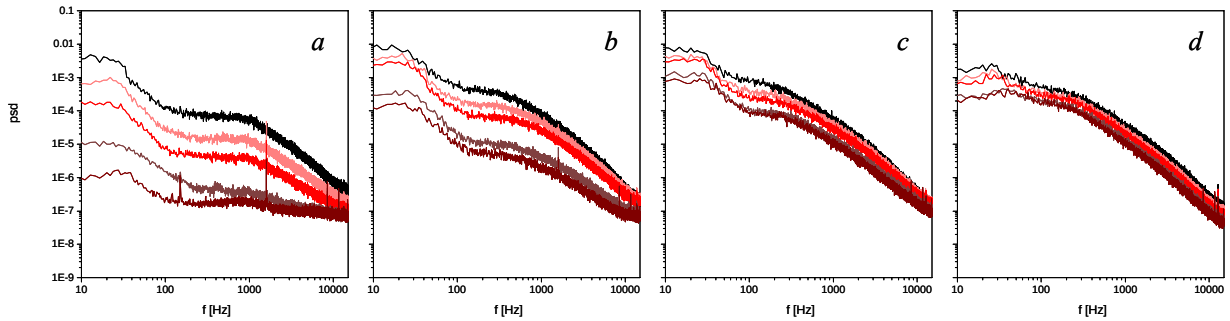

Figure 9. *Power spectra of the velocity fluctuations (M = 0.3 and γ = 139°) for the baseline flow (—) and controlled flows measured by HW1 at y/R = -0.042 (a), HW2 at y/R = -0.17 (b), HW3 at y/R = -0.42 (c), and HW4 at y/R = -0.58 (d). The spectra of the controlled flow for increased jet momentum coefficient are marked by increasingly darker red traces.*

energy within the wake over the entire streamwise measurement domain. As shown in a planar shear layer by earlier investigations (Vukasinovic, Glezer, and Rusak 2007), for a given jet momentum coefficient the streamwise suppression of TKE decreases with increasing distance from the control source which is a direct consequence of the enhanced dissipation within the flow. The present data also indicate that additional reduction can be attained a higher actuation power (the present measurements are taken at the maximum available actuation level $C_\mu = 5.6 \cdot 10^{-4}$).

Comparison of the static pressure distributions in the presence and the absence of the actuation shows consistent separation delay effects across the optical window, where the magnitude of the separation delay is about 10° at $M = 0.3$. This effect is illustrated in Figure 10, where static pressure distributions in each of the three measurement planes are shown for $\gamma = 139°$ and M = 0.3 and 0.4. In the presence of actuation the alteration of the baseline pressure distributions begins at about 75° i.e., upstream from the turret apex. The acceleration of the outer flow extends the pressure recovery in the downstream direction, which in turn delays the separation of the boundary layer. The separation delay effect becomes less pronounced with an increase in M due to the effective decrease in jet momentum coefficient, as can be shown by comparison of the distributions in all three measurement planes for M = 0.3 and 0.4. Although separation

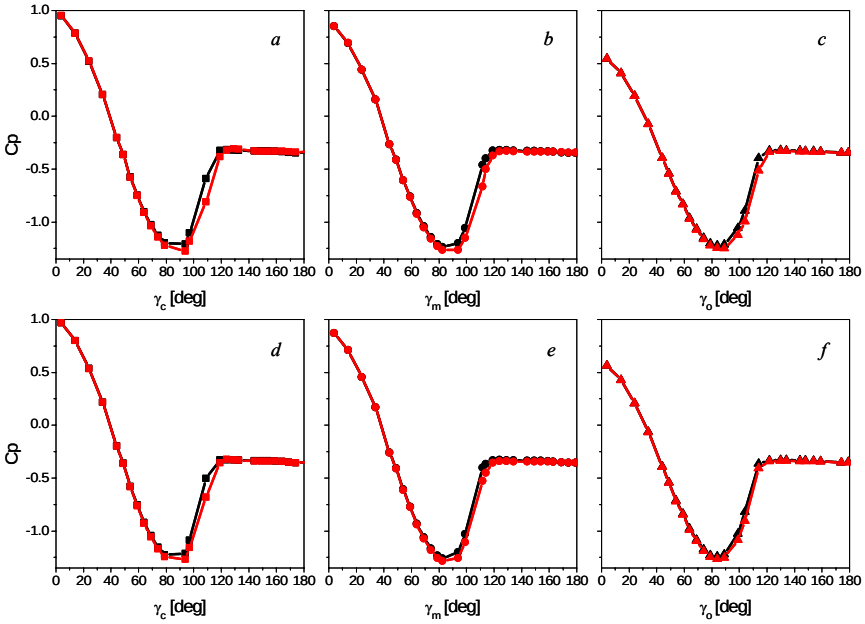

Figure 10. *Static pressure distributions for the baseline flow (—) at actuated (—) flows at γ = 139° in the central (a,d), middle (b,e), and the outer (c,f) planes at M = 0.3 (a-c) and 0.4 (d-f).*

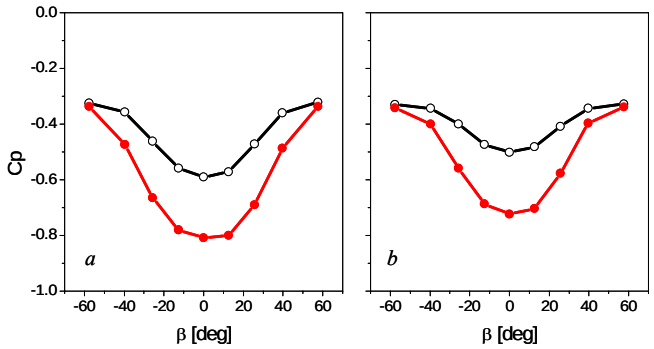

Figure 11. *Pressure distributions about the optical window center ($\beta = 0$) at window elevation $\gamma = 139°$ for the baseline flow (—) at actuated (—) flows at $M = 0.3$ (a) and 0.4 (b).*

control typically results in some suppression of turbulent fluctuations in the separated flow, the work of Vukasinovic, Glezer, and Rusak (2007) has shown that dissipative actuation upstream of a separating shear layer off the backward-facing step leads to the disruption of turbulent kinetic energy budget in the ensuing flow. Active suppression of turbulent kinetic energy within the shear layer can be achieved even in the absence of significant separation delay, as it was demonstrated in a shear layer separating from a backwards facing step.

Pressure distributions just upstream of the optical window are shown in Figure 11 for the flow conditions in Figure 10. Both baseline and actuated pressure distributions indicate symmetric pressure distributions about the center plane of the window ($\beta = 0$, Figure 1). At both Mach numbers, the baseline flow upstream of the window is attached and similar to the data shown in Figure 4 above, the inverted bell-shape profile indicates that the flow first separates at the spanwise edges of the window, while the flow over front central part of the window remains attached. In the presence of actuation at $M = 0.3$ (Figure 11*a*), the largest reduction in pressure is achieved at the center of the window but there is a nearly-uniform separation delay over about the center half of the window span. Farther outboard towards the edges of the window ($\beta = \pm 57.7°$), there is a sharper decrease in the delay of separation. A similar effect is also seen for $M = 0.4$ (Figure 11*b*).

The differences between the baseline and controlled flows are evident from spectra of velocity fluctuations measured using hot wire anemometry. Overall, the spectral analysis shows a significant broadband reduction in the energy of motions within the separated shear layer (it should be pointed out that for a given downstream position, the energy balance depends on the cross-stream elevation within the shear layer). Figure 12 shows power spectra of velocity fluctuations measured in the central zone of the baseline shear layer at all four measurement locations and among three Mach numbers tested, $M = 0.3$, 0.4, and 0.5. Closest to the control origin (Figure 12*a*), there is a dominant broadband suppression of fluctuation energy at $M = 0.3$;

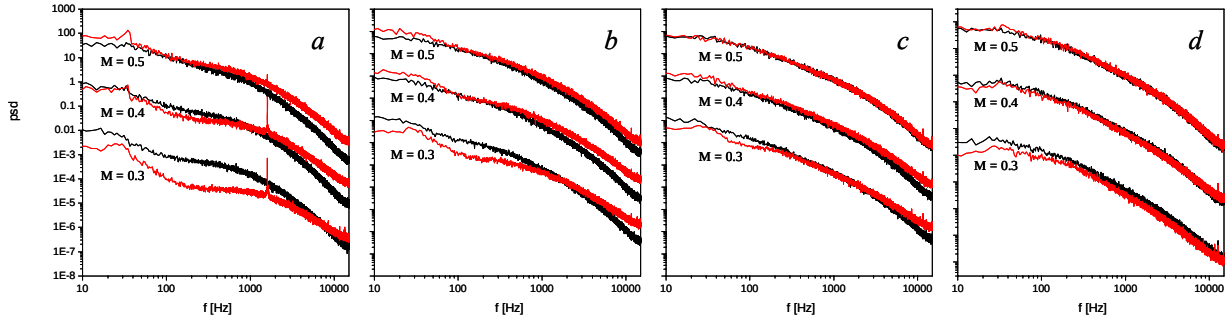

Figure 12. *Power spectra of the velocity fluctuations for the baseline (—) and actuated (—) flows ($\gamma = 139°$) measured by HW1 at y/R = -0.083 (a), HW2 at y/R = -0.25 (b), HW3 at y/R = -0.58 (c), and HW4 at y/R = -0.75 (d) for M = 0.3, 0.4, and 0.5.*

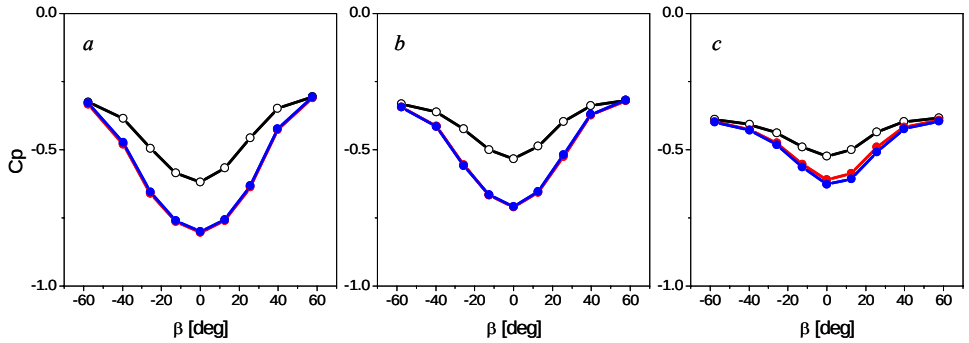

Figure 13. *Pressure distributions about the optical window center (β = 0) at window elevation γ = 137° for the baseline (—) at actuated flows by: 36(—) and 24 (—) element actuator arrays at M = 0.3 (a), 0.4 (b), and 0.5 (c).*

similar, but weaker suppression of energy at large scales at M = 0.4, but accompanied with an increase in energy at the small-scale motions. Ultimately, an increase in the energy spreads towards the lower frequencies at the highest Mach number flow, and becomes the dominant effect of the flow control. The effect at M = 0.3 at the next downstream location (Figure 12*b*) is similar to the effect at M = 0.4 at the previous location, while the effect at M = 0.4 is similar to the previous location M = 0.5, and so on. It is a consistent indicator of the weakening effect in the downstream direction (due to the dissipation of the control jets), and with the increased free-stream speed (due to decreased jet momentum coefficient). By the measurement location HW3 (Figure 12*c*), virtually no effect is seen at M = 0.5, while the flows at M = 0.3 and 0.4 exhibit some increase in energy at the small scales and some decrease of energy at the large scales. At the farthest measurement location (Figure 12*d*), decrease of the fluctuating energy is still present at M = 0.3. Thus, the strongest effect of the flow control remains always closest to the control source origin, i.e., over the optical window, regardless of the free stream speed.

The effectiveness of a smaller spanwise array of actuators was investigated by comparing the effects of the center 24-element segment of the 36-elemenet actuator array in Figure 1. The resulting pressure distributions upstream of the optical window are shown in Figure 13 for the window elevation angle γ = 137° at M = 0.3, 0.4, and 0.5. These data show that in all cases the effect of the smaller actuator array is virtually identical, implying that the outboard actuator segment on each side is not very effective ostensibly due to the influence of the necklace vortices that are involved in the separation of the cylinder support. It is also noted that the actuation effect becomes more localized about the window center as M increases. Similarly, the effectiveness of the smaller array actuation is evaluated at three window elevation angles γ = 130°, 142°, and 149°, as shown in Figure 14. At γ = 130° (Figure 14*a*), the baseline flow is attached in front of the optical window, and the actuation delays the separation uniformly across the window even with the 24-element array. At γ = 142° (Figure 14*b*), the baseline flow is separated

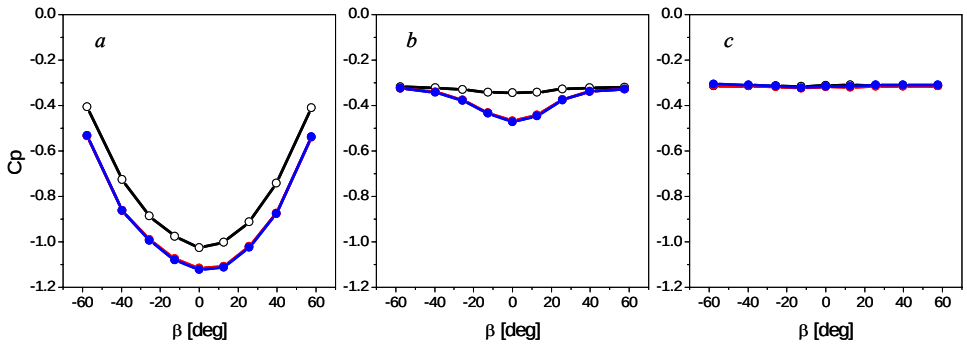

Figure 14. *Pressure distributions about the optical window center (β = 0) at M = 0.3 and window elevations γ = 130° (a), 142° (b), and 149° (c) for the baseline (—) and actuated flows using 36 (—) and 24 (—) element actuator arrays.*

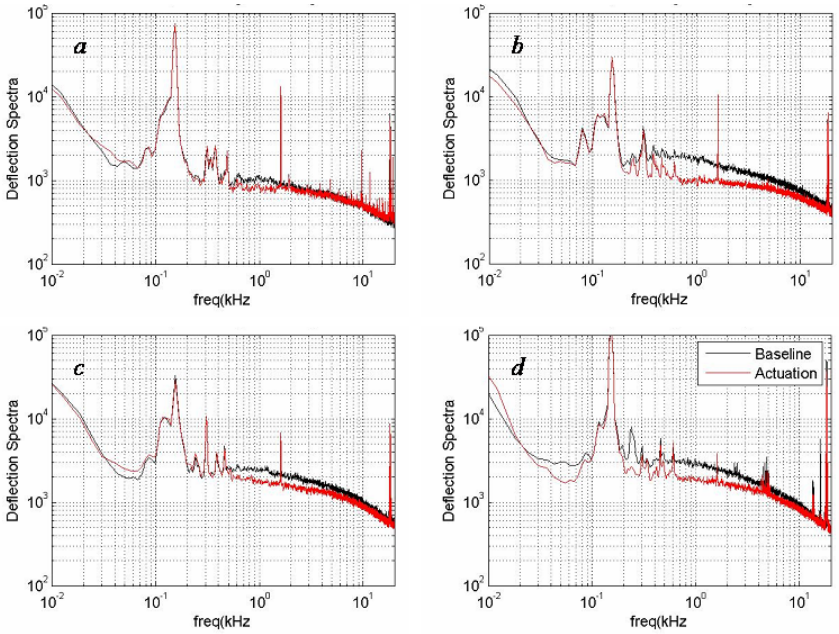

Figure 15. *Spectra of the optical deflection for the baseline (—) and actuated (—) flows at M = 0.3 and γ = 129° (a), 136° (b), 143° (c), and 148° (d).*

upstream of the optical window, but the actuation delays the separation across the upstream edge of the window. At $\gamma = 149°$ (Figure 14*c*), the flow remains separated over the upstream edge of the window even in the presence of actuation (indicating that the actuation should be applied farther upstream), although, as indicated by the measured velocity spectra, the flow fluctuations within the separated domain are significantly suppressed.

The magnitude of optical distortions that would be encountered by a laser beam emerging from the optical window was measured directly using a Malley probe. The Malley probe (MP) sensor records time series of deflection angles of two small diameter laser beams and reconstructs optical distortions using a frozen field hypothesis, see Gordeyev, Hayden and Jumper (2007) for a complete description of the Malley probe principle of operation. Spectra of deflection angles measured in the baseline and actuated flows at $M = 0.3$ are shown in Figure 15 for the window elevation angles $\gamma = 129°$, 136°, 143°, and 148°. It should be noted (as is evident from these data) that the spectral optical content below 500 Hz is entirely masked by the tunnel environment that, in addition to aero-optical effects, also include vibrations of the optical hardware and of the model, as already discussed in Section III. These vibrations which are manifested by strong spectral peaks below 500 Hz completely overwhelm the optical signal and render the raw data unusable at these frequencies for the purpose of active flow control evaluation.

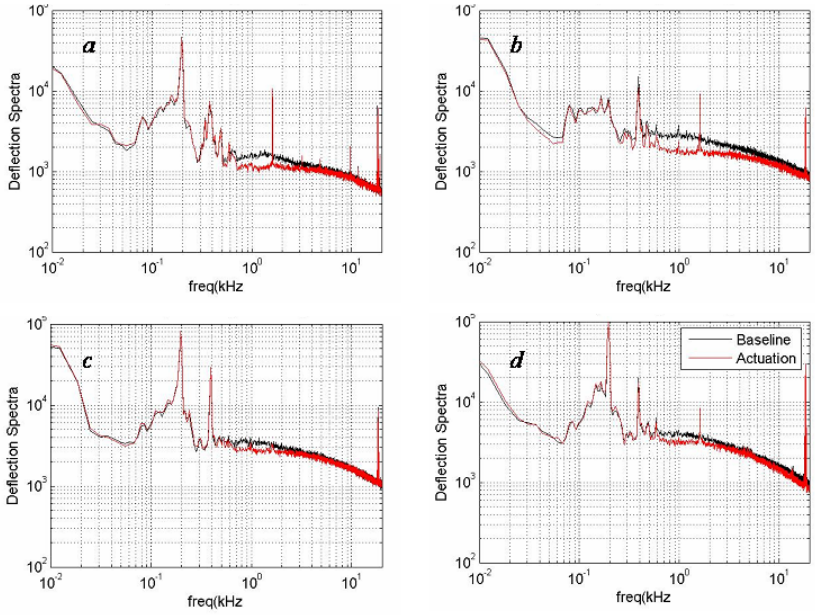

Figure 16. *Spectra of the optical deflection for the baseline (—) and actuated (—) flows at M = 0.4 and γ = 129° (a), 136° (b), 143° (c), and 148° (d).*

However, another control approach in reducing the optical aberrations at these low frequencies could involve both active flow control suppression and adaptive-optics correction of aberrations (including the tip/tilt correction using a fast steering mirror). Assuming that most of the "low-frequency" aberrations below 500 Hz could be mitigated by the adaptive optics system, current results can be viewed as additional suppression of optical aberrations beyond the range of optical corrections. In addition, the present MP measurements are taken with a sampling rate of 50 kHz, which imposes an upper frequency band limit around 25 kHz. As a result, the present MP data can only be used to assess the effectiveness of the flow control actuation within the band $500 < f < 25{,}000$ Hz. Except for $\gamma = 143°$ at $M = 0.4$, every actuated spectra in Figure 15 show a spike in the actuator-spectra at 1.6 kHz to a greater or lesser extent. This spike indicates that the actuators are introducing well-defined structures into the boundary layer that are responsible for keeping the flow attached (i.e. preventing the separation otherwise present in the baseline flow), and actuation-induced structures induce narrow-band aberrations as will be discussed in more details below. It is noteworthy that the magnitude of this actuation-frequency peak decreases with increasing elevation angle, as the vortical motions that are induced by the actuation dissipate faster within the stronger separated base flow at the higher elevation angles. The most important effect of the actuation-induced small-scale motions on the aero-optical environment around the window is the reduction in the energy of the deflection angles within the entire frequency band that is resolved by the MP measurements at all elevation angles. Albeit actuation introduces aberrating structures into the flow at the actuator frequency, the overall effect of the actuation is a broad reduction in the jitter (and concomitant contribution to OPD_{rms}) over the broad frequency range. In particular, the reduction in deflection angle spectra at frequencies between 0.2 and 10 kHz has the largest effect on the OPD_{rms}, see Appendix for details These spectra also demonstrate that the actuation mostly affects frequencies below the actuation frequency of 1.6 kHz and at higher frequencies the actuation spectra are affected less by the actuation and approach the spectra of the baseline. In the present measurements, the reduction in spectra of deflection angles is most-significant at $\gamma = 136°$ (Figure 15*b*). It is interesting to note that the smallest suppression is measured at the lowest elevation angle $\gamma = 129°$ (Figure 15*a*), but that is attributed to a weak shear layer since the flow separates at about $\gamma_s = 120°$ (Figure 3*a*). It should also be noted that the absolute magnitude of the baseline spectrum at $\gamma = 129°$ is about an order of magnitude lower than the corresponding baseline spectrum at $\gamma = 136°$ (Figure 15*b*). Similar energy suppression by flow control is also measured at higher Mach-

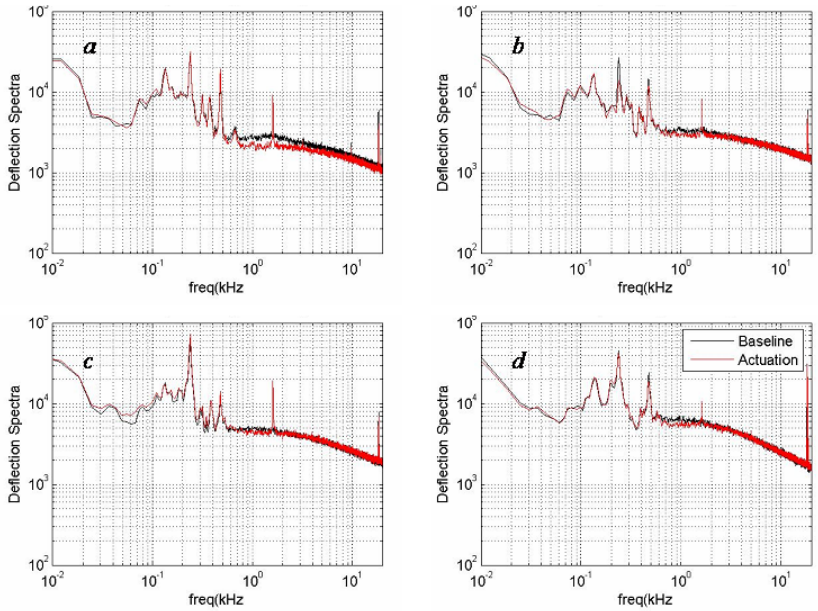

Figure 17. *Spectra of the optical deflection for the baseline (—) and actuated (—) flows at M = 0.5 and γ = 129° (a), 136° (b), 143° (c), and 148° (d).*

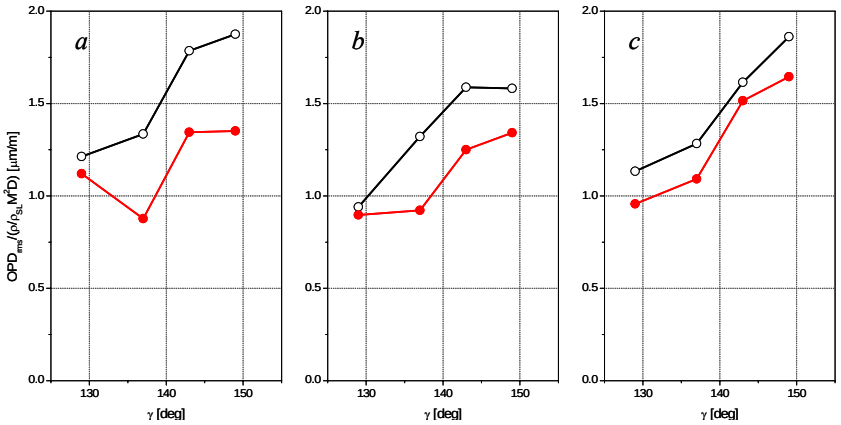

Figure 18. *Normalized baseline (○) and controlled-flow (●, case 1) optical data, OPDrms /(ρM²D), as a function of elevation angle γ for all Mach numbers M = 0.3 (a), 0.4 (b), and 0.5 (c).*

number flows, at M = 0.4 (Figure 16) and 0.5 (Figure 17), but with weakening effectiveness as the actuators' momentum coefficient decreases with increasing M.

Finally, it is of interest to quantify the amount of aberration that the introduction of the 1.6 kHz structures has on the optical environment. To address this question, a narrow band-pass filter was placed around the each jitter spectra centered on 1.6 kHz for the *case 1* data and the OPD_{rms} computed for only the notched spectra. The contribution of these aberrating structures to overall OPD_{rms} were found to range from 1% to 7% of the no-notch OPD_{rms}. Hence, in the case of γ = 137° at M = 0.3, for example, the 34 % reduction in OPD_{rms} could have been a 41% reduction had the optical effect from 1.6 kHz aberrating structures been somehow removed.

The measured deflection spectra were band-pass filtered within the above-stated range and the levels of optical distortions were calculated for each actuation case and compared to the corresponding baseline flow, as discussed in Section II and Appendix. Figure 18 shows the comparison of the *case 1* actuation to the baseline for each elevation angle and all three Mach numbers in a non-dimensional form. Common feature is that the actuation yielded suppression in optical aberrations for all the flow conditions. It should be also noted that in many cases the improvement over the baseline was quite large. At M = 0.3, the reduction in OPD_{rms} at γ = 137°, for example, for *case 1* yielded a 34% improvement and at M = 0.4 the improvement dropped by only 4% to a 30% improvement. This reduction in OPD_{rms} is even more significant to the far-field intensity, since the far-field intensity improvement goes approximately as

$$\frac{I}{I_0} = \exp\left\{-\left(\frac{2\pi OPD_{rms}}{\lambda}\right)^2\right\}$$

where I is the on-axis intensity after tilt removal, divided by the diffraction limited intensity, I_0, and λ is the laser wavelength.

All the results are presented in Table 1, where actuation using the full set of actuators is labeled as *case 1*, and spanwise-limited actuation using the 24 central actuators is labeled as *case 2*. Full actuation (*case 1*) was tested at all four window elevation angles and at each Mach number, while *case 2* was tested at two elevation angles for M = 0.3 and 0.4, and one elevation angle at M = 0.5. As already discussed in conjunction with Figure 16, the smallest relative improvement in optical distortions within the present spectral band is measured at the lowest elevation angle at M = 0.3, but significant suppression is measured at all other elevation angles where the shear layer over optical window is more developed. Very similar, but slightly weaker effects on aberrations' suppression are achieved at M = 0.4. The overall effect weakens further at the highest Mach-number flow M = 0.5, but the bandwidth-limited measured suppression is still

notable. When assessing the impact of reduced spatial distribution of actuators, by comparing cases 1 and 2, no significant difference is observed, as the measured suppression by the spanwise-limited distribution of actuators is either slightly weaker, or even slightly stronger than in the case of full actuation. This finding suggests a possible redistribution of the control sources for future tests. It is should be also pointed out that although the active flow control at $M = 0.3$ and $\gamma = 149°$ does not effect the separation off the turret (see Figure 14*c*), measured aberrations by the Malley probe indicate the resulting suppression of optical aberrations of about 30% (Table 1). This finding shows that the effect of fluidic active flow control on optical aberrations is not exclusively expressed through separation delay, but it induces an active suppression of turbulent fluctuations even in the absence of separation delay.

Table 1. *Relative improvement in optical distortions as measured by RMS of the OPD in the actuated flows relative to the baseline flows for different elevation angles γ based on spectral data within the range of the MP sensor $0.5 < f < 25$ kHz.*

	γ [deg]	129	136	143	149
M = 0.3	case 1	8%	34%	24%	28%
	case 2	-	31%	-	37%
M = 0.4	case 1	5%	30%	21%	15%
	case 2	-	-	24%	12%
M = 0.5	case 1	20%	15%	6%	12%
	case 2	-	12%	-	-

V. Conclusions

The effectiveness of direct, dissipative small-scale actuation for suppression of optical aberrations within the separated flow over the conformal optical window mounted in the hemispherical cap of a cylindrical turret model is investigated at $M = 0.3$ and $Re_D = 4.46 \cdot 10^6$, with additional tests done at $M = 0.4$ and 0.5. The effects of actuation on the base flow at several elevation angles of the optical window are assessed from surface oil visualization, static pressure distributions, and hot-film measurements within the separated flow domain. Suppression of optical distortions across the separated flow is evaluated directly using the Malley probe sensor.

The topology of the baseline flow at $M = 0.3$ indicates that the near-wake flow is dominated by the separation off the hemispherical cap of the turret. The flow separates first near the outer spanwise edges of the hemisphere, and the separation progresses towards the center plane, such that the flow remains attached farthest along the plane of symmetry. The separated wake downstream of the turret reattaches to the base plane of the turret at a nominal distance of $1.3R$ downstream from its downstream juncture. Surface oil visualization has shown that the recirculating flow domain is bounded along its spanwise edges by two separate, narrower recirculating domains that are induced by separation off the turret's cylinder support. The flow separation along the cylinder support is amplified by interaction with the necklace vortex that forms at the juncture between the cylinder and the support plane.

Direct small-scale, dissipative actuation using arrays of streamwise rectangular synthetic jets mounted around the upstream perimeter of the optical window leads to a significant separation delay on the window's surface. The extent of the separation delay varies with the elevation angle γ of the window, and can extend up to 10^o at $\gamma = 139^o$. Furthermore (and perhaps more importantly), spectra of the streamwise velocity fluctuations show that the dissipative actuation results in a substantial broad-band suppression of the turbulent kinetic energy within the near wake and in particular the energy that is associated with large coherent vortical structures. Although this attenuation is not a direct measure of the reduction in aero-optical aberrations, it is indicative of the overall reduction in the characteristic length scales within the separated flow domain. Direct optical measurements at a free-stream Mach number $M = 0.3$ show that the actuation leads to a suppression of at least 30% in optical aberration as measured within the frequency band $0.5 < f < 25$ kHz (at the low end this band is limited by the tunnel's optical contamination and vibrations). Under the assumption that any existing aberrations below the lower limit of 500 Hz could be mitigated by means of a conventional adaptive optic system, the current results can be viewed as additional suppression of optical aberrations beyond the range of optical corrections. The broad band turbulent energy suppression that is evident from hot wire velocity spectra suggests that the actual reduction in optical aberrations may be higher. Additional measurements at $M = 0.4$ and 0.5 show similar trends albeit somewhat less effective in terms of separation delay and suppression of optical aberrations. The actuation effects at these higher Mach numbers are apparently limited by the strength of the present actuators and the precipitous decrease in jet momentum coefficient with Mach number. The suppression of optical aberrations (beyond the adaptive optics correction) is at least 20% and 10% for free stream Mach numbers M = 0.4, 0.5, respectively. It is noteworthy that the same suppression of optical aberrations was attained with the central 2/3 subset of the jet actuator array upstream of the optical window and therefore with about 2/3 of the actuation power. Finally, as the structures introduced into the flow by the actuation are so narrowly centered at the actuation frequency, it is believed that they could be removed using a feed-forward, adaptive-optics approach similar to that demonstrated with a regularized shear layer (Nightingale *et al.* 2008).

Appendix

Relation between deflection-angle spectra and OPD_{rms}

Mechanically-induced vibrations from the tunnel motor impose significant amounts of contamination at the low-frequency end of the deflection-angle spectra and partially corrupt the aero-optical signal. In order to remove this mechanical-vibration corruption, one needs to know the correct, uncorrupted behavior of the deflection-angle spectrum at the low-frequency end to properly filter it out.

To derive a proper high-pass filter, it is helpful to revisit how Malley probe data are used to construct a meaningful optical figure-of-merit. Malley probes measure 1-D jitter/deflection-angle spectra, $P_\theta(f) = \left\langle \hat{\theta}(f)\hat{\theta}^*(f) \right\rangle$, but a typical figure-of-merit for aero-optics is OPD_{rms} for a given aperture size, Ap. These quantities are related as follows: Since the square of the RMS Optical Path Difference is identical to the square of the RMS wavefront distortion from its mean, i.e., $OPD_{rms}^2 \equiv W_{rms}^2$, the OPD_{rms} is related to the 1-D wavefront power spectrum, $P_W(k) = \left\langle \hat{W}(k)\hat{W}^*(k) \right\rangle$, as

$$OPD_{rms}^2 \equiv \frac{1}{2\pi}\int_{-\infty}^{\infty} P_W(k)dk\,, \tag{1}$$

where $\hat{W}(k)$ is the Fourier transform of a 1-D wavefront distortion, *W(x)*. However, the jitter/deflection angle, θ, is the spatial derivative in the streamwise direction of the wavefront,

$$\theta(x = U_c t) = \frac{dW(x = -U_c t)}{dx} = -\frac{1}{U_c}\frac{dW(t)}{dt}\,.$$

Here the frozen-flow convective hypothesis is applied with U_c being the convective speed. The deflection power spectrum can be computed from the wavefront power spectrum as $P_\theta(f) = \left(\frac{2\pi f}{U_c}\right)^2 P_W(f)$. Substituting this expression into Eq. (1) we get,

$$OPD_{rms}^2 = \frac{1}{2\pi}\int_{-\infty}^{\infty} P_W(k)dk = \int_{-\infty}^{\infty} P_W(f)df = \int_{-\infty}^{\infty}\left(\frac{U_c}{2\pi f}\right)^2 P_\theta(f)df = U_c^2\int_{-\infty}^{\infty}\frac{P_\theta(f)}{(2\pi f)^2}df$$

The derived expression is valid only for an infinite aperture. It was shown that for finite apertures (Vukasinovic *et al.* 2008), the above expression should be modified by including a 1-D aperture filter, *AF*(*Ap*, *f*), see Figure A1*a*,

$$OPD_{rms}^2(Ap) = U_c^2\int_{-\infty}^{\infty} AF(Ap,f)\frac{P_\theta(f)}{(2\pi f)^2}df = \int_0^{\infty} G(Ap,f)P_\theta(f)df\,, \tag{2}$$

where $G(Ap,f) = \frac{2U_c^2}{(2\pi f)^2}AF(Ap,f)$ is a transfer function between the deflection angle spectrum and the apertured $OPD_{rms}(Ap)$. Figure A1*a* shows the transfer function, *G*(*f*), normalized by the maximum value for *Ap* = 1/3 *D* as a function of $St = fD/U_\infty$, where *D* is a turret diameter and U_0 is the freestream speed (U_c = 0.8U_0). The normalized cumulative transfer function, $CG(f) = \int_o^f G(x)dx \Big/ \int_o^\infty G(x)dx$, is plotted in Figure A1*b*. The transfer function is essentially a band-pass filter, centered about *St* = 3. The low-frequency cut-off is due to aperture effects, where very low frequencies are present essentially as tip-tilt and therefore are removed from the final result under the presumption that a Fast Steering Mirror would be present in the beam-control system for a laser. The high-frequency cut-off is due to the integral relation between the jitter/deflection-angle signal and the wavefront. Therefore, Eq. (2) shows that the measured optical quantity, the jitter/deflection-angle spectrum, should be, in effect, *band-pass filtered* in order to calculate the level of aero-optical aberrations, OPD_{rms}, for a given aperture size.

From the cumulative function, *CG*(*t*), see Figure A1*b*, it is clear that for this aperture, 95% of the "filtered energy" is located between *St* = 1 and 60. Therefore, the exact shape of the low-

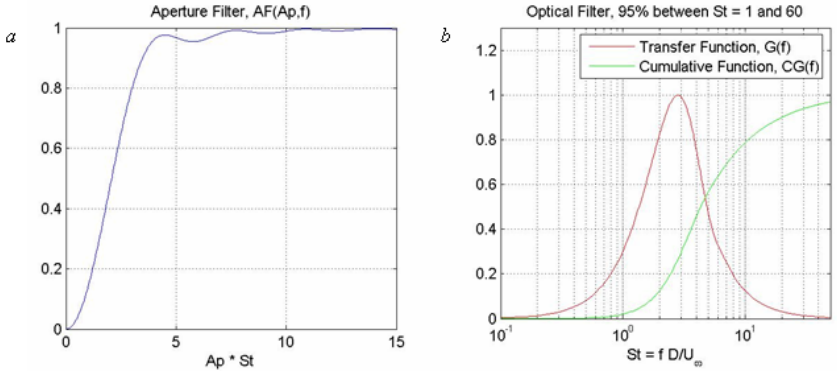

Figure A1. *Aperture filter (a) and optical transfer and cumulative functions (b).*

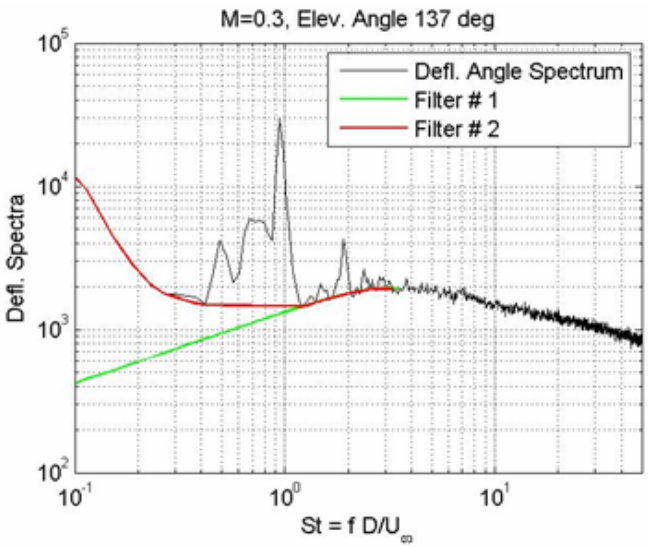

Figure A2. *Deflection angle spectrum and two different low-pass filters.*

pass filter (or more accurately, the fit) which is applied to the measured deflection angles to compensate for vibration contamination is in fact *irrelevant* below St = 1 (and above St = 60) as long as all non-physical components, like vibrations, are removed or highly suppressed by the empirical low-pass filter. Direct numerical calculations confirm these results. Two different filters were applied to remove vibration-related low frequencies, see Figure A2. The resulting OPD_{rms} after applying these two filters differ by less than 6%. So, all data reported below were processed by applying Filter # 1.

High-pass filter # 1, $F(f)$, was constructed as follows,

$$F(f) = \begin{cases} \dfrac{P_\theta(f_{cut})\left(\dfrac{f}{f_{cut}}\right)^n}{P_\theta(f)}, & f < f_{cut} \\ 1, & f \geq f_{cut} \end{cases}.$$

The cut-off frequency was chosen to be $f_{cut}D/U_\infty = 4.0$. The filter was then applied to the time-dependent data as discussed earlier. Several values of n between 1 and 2 were tested and it was found that the resulting apertured OPD_{rms} did not change much, so the conservative value of n = 1 was chosen for the high-pass filter $G(f)$.

Acknowledgment

This work has been supported by the Air Force Research Laboratory.

References

Amitay, M. and Glezer, A., "Role of actuation frequency in controlled flow reattachment over a stalled airfoil", *AIAA Journal*, Vol. 40, 2002, pp.209-216.

Cress, J., Gordeyev, S., Jumper, E., Ng, T., and Cain, A., "Similarities and differences in aero-optical structure over cylindrical and hemispherical turrets with a flat window", *AIAA Paper* 2007-0326, 2007.

de Jonckheere, R., Russell, J. J., and Chou, D. C., "High subsonic flowfield measurements and turbulent flow analysis around a turret proturberance", *AIAA Paper* 82-0057, 1982.

Fitzgerald, E. J. and Jumper E. J., "The optical distortion mechanism in a nearly incompressible free shear layer," *J. Fluid Mech.*, Vol. 512, 2004, pp. 153-189.

Gilbert, J. and Otten, L. J. (eds), *Aero-Optical Phenomena*, Progress in Astronautics and Aeronautics, Vol. 80, AIAA, New York, 1982.

Gordeyev, S., Hayden, T., and Jumper, E., "Aero-optical and flow measurements over a flat-windowed turret", *AIAA J.*, Vol. 45, 2007, pp. 347-357.

Gordeyev, S., Jumper, E. J., Ng, T. T., and Cain, A. B., "The optical environment of a cylindrical turret with a flat window and the impact of passive control devices", *AIAA Paper* 2005-4657, 2005.

Gordeyev, S., Post, M. L., McLaughlin, T., Ceniceros, J., and Jumper, E. J., "Aero-optical environment around a conformal-window turret", AIAA J., Vol. 45, 2007, pp. 1514-1524.

Jumper, E. J., and Fitzgerald, E. J., "Recent advances in aero-optics", *Progress in Aerospace Sciences*, Vol. **37**, 2001, pp.299-339.

Leder, A., Grebin, U., Hassel, E., Kashkoul, Y., and Ackl A., "3D-Flow structures behind a circular cylinder with hemispherical head geometry", *Proc. Appl. Math. Mech,.* Vol. 3, 2003, pp 40–43.

Manhart, M., "Vortex shedding from a hemisphere in a turbulent boundary layer", *Theoret. Comput. Fluid Dynamics*, Vol. 12, 1998, pp. 1–28.

Morgan, P. E. and Visbal, M. R., "Numerical simulations investigating control of flow over a turret", *AIAA Paper* 2009-574, 2009.

Nightingale, A., Mitchell, B., Goodwine, B., and Jumper, E., "Feedforward adaptive-optic mitigation of aero-optic disturbances", *AIAA Paper* 2008-4211, 2008.

Purhoit, S. C., Shang, J. S., and Hankey, W. L., "Effect of suction on the wake structure of a three-dimensional turret", *AIAA Paper* 83-1738, 1983.

Siegenthaler, J., Gordeyev, S., and Jumper, E., "Shear layers and aperture effects for aero-optics", *AIAA Paper* 2005-4772, 2005.

Smith, D. R., Amitay, M., Kibens, V., Parekh, D., and Glezer, A., "Modification of lifting body aerodynamics using synthetic jet actuators", *AIAA Paper* 1998-0209, 1998.

Snyder, C. H., Franke, M. E., and Masquelier, M. L., "Wind-tunnel tests of an aircraft turret model", *J. Aircraft*, Vol. 37, 2000, pp. 368-376.

Sutton, G. "Aero-optical foundations and applications", *AIAA J.*, Vol, 23, 1985, pp 1525-1537.

Tatarskii, V. I. and Zavorotnyi, V. U, "Wave propagation in random media with fluctuating turbulent parameters,", *J. Opt. Soc. Am. A*, Vol. 2, No. 12, 1985, pp. 2069-2076.

Vukasinovic, B. and Glezer, A., "Control of a separating flow over a turret*", AIAA Paper* 2007-4506, 2007.

Vukasinovic, B., Brzozowski, D., Glezer, A., Bower, W., and Kibens, V, "Separation control over a surface-mounted hemispherical shell", *AIAA Paper 2005-4878*, 2005.

Vukasinovic, B., Glezer, A., and Rusak, Z., "Experimental and numerical investigation of controlled, small-scale motions in a turbulent shear layer*", Proc. 3rd International Symposium of Integrating CFD and Experiments in Aerodynamics*, June 2007, U.S. AFA, CO, USA.

Vukasinovic, B., Glezer, A., Gordeyev, S., Jumper, E., and Kibens, V., "Active control and optical diagnostics of the flow over a hemispherical turret, *AIAA Paper* 2009-598, 2008.

Woszidlo, R., Taubert, L., and Wygnanski, I., "Manipulating the flow over spherical protuberances in a turbulent boundary layer", *AIAA J.*, Vol. 47, 2009, pp. 437-450.